A cortical motor nucleus drives the basal ganglia-recipient thalamus in singing birds

Jesse H. Goldberg and Michale S. Fee

Supplementary Material

Supplementary Fig. 1. Thalamic firing patterns during singing. (**a**) Schematic of the experimental design for recording pallidal axon terminals and antidromically-identified LMAN-projecting neurons in DLM, highlighting regions of interest shown at right. (**b**) Small electrolytic lesions (red arrowhead) confirmed the location of the recording electrode in DLM. (c**)** Electrolytic lesions and tracks confirm placement of bipolar stimulating electrodes in LMAN. (**d–e**) During singing, high tonic discharge (HTD) events, defined as firing events exceeding 250 Hz, were not preceded nor followed by periods of quiescence. (**d**) Plot of instantaneous firing rate (IFR) functions aligned to HTD onsets (gray trace). Each trace represents the average for one DLM neuron. Also shown is the average over all neurons (n = 29, black trace). Note that HTDs were generated from a baseline firing rate of over 100 Hz. Instantaneous firing rate is defined between every pair of consecutive spikes as the inverse of the interspike interval (see Methods). Thus the average interspike interval of a DLM neuron prior to the onset of HTDs was less than 10 ms. (**e**) Histogram of HTD-onsets, aligned to HTD offsets. (This is analogous to a spike-train autocorrelation function.) Note that HTDs did not exhibit refractory periods. (**f–g**) The threshold at which HTDs were defined did not affect our results. (**f**) HTD onset aligned IFRs are plotted as in panel d for HTD thresholds of 200 Hz (red), 250 Hz (blue) and 300 Hz (black). Each trace is the average of 29 DLM

neurons during singing. (**g**) The incidence of HTDs during non-singing is compared to that during singing for HTD thresholds examined in panel f.

Supplementary Fig. 2. Thalamic firing patterns in plastic song birds. (**a**) Voltage trace and IFR are plotted beneath the spectrogram of a plastic song bird (dph 65). Syllable segmentation and labels are plotted beneath the spectrogram. (**b**) Antidromic identification and collision testing of the neuron shown in panel a. (**c**) Expanded view of the voltage, IFR and spectrogram from above (indicated by motif 'abc' labeled red bars). (**d**) Spike raster showing activity of this neuron during 23 renditions of the motif; *bottom*: the rate histogram compiled from the raster plot. Blue and red asterices indicate significant maxima and minima in firing rate (see methods). (**e**) Syllable onset-aligned rate histograms for the neuron in shown in panel a (top) and for all DLM neurons recorded in plastic song birds (bottom). Dark lines and shaded areas are mean ± s.e.m. (**f**) Syllable offset-aligned rate histograms, plotted as in e. (**g**) Histograms showing the incidence of significant peaks (left) and troughs (right) compiled from syllable-aligned rate histograms (see methods). Note that significant modulations occur throughout the syllables, not just at syllable onsets.

To compare the syllable-locked rate modulations in DLM neurons to those observed in LMAN and Area X, we computed correlation coefficients (CCs) between spike trains on a trial (syllables)-by trial basis were computed exactly as described[1]. We found that CCs were significant but weak (CCs = 0.058 ± 0.056, n = 15 DLM neurons), similar to what was previously observed in LMAN neurons (0.054 ± 0.034)[2] and pallidal terminals (0.050 ± 0.45)[1] at the plastic song stage.

Supplementary Fig. 3. Firing patterns of Area X output (~GPi-like) neurons during subsong. Putative DLM-projecting pallidal neurons in Area X were previously shown to be indistinguishable from pallidal terminals recorded in DLM[1]. Here these neurons, which resemble neurons in the primate internal pallidal segment (GPi), were recorded during vocal babbling in juvenile birds to verify that the observed firing patterns of pallidal terminals recorded in DLM were indeed reflective of the GPi-like neurons in Area X (see Methods). (**a**) Instantaneous firing rate of a GPi-like neuron (bottom) and spectrogram of subsong vocalization (top, dph 49). (**b**) Average firing rates ± s.e.m. of ~GPi-like neurons during non-singing and singing epochs (n = 17 cells). (**c**) Example of the same neuron (panel a) exhibiting a firing-rate increase at syllable onsets (note two syllables). Data are an expanded view of the period marked by a gray bar in panel a. (**d**) Syllable onset-aligned rate histograms for the neuron in shown in panel a (top) and for all GPi-like neurons in Area X (bottom). (**e**) Syllable offset-aligned rate histograms. Data shown as in panel d. As a group, GPi-like neurons in Area X exhibited increased average firing rates during singing (non-singing: 141.2 ± 6.8 Hz vs. singing: 257.4 ± 10.2 Hz, $p<0.001$ paired tests, n = 17/17 cells), a peak in firing rate prior to syllable onsets (rate increase of 18.5 ± 2.3 Hz, beginning 37.0 ± 3.3 ms prior to onsets, $p<0.05$ in 16/17 cells), and a decrease in firing rate prior to syllable offsets (rate decrease of 10.0 ± 1.3 Hz, beginning 67.5 ± 6.5 ms prior to offsets, $P < 0.05$ in 10/17cells).

Supplementary Fig. 4. Template-matching spike-sorting algorithm used to detect spike overlaps in the paired pallidothalamic recordings. (**a**) Scatter plot of mean firing

rate during singing versus spike duration for all units recorded in DLM. Two clusters of units are apparent: (1) thin spiking units discharging at high average rates (categorized as pallidal axon terminals, red circles), and wider spiking units discharging at lower rates (categorized as DLM neurons, blue circles). Many DLM neurons were antidromically identified LMAN-projecting (blue filled circles). (**b**) Left, example voltage waveforms of three paired recordings. Pallidal and thalamic spikes are labeled with red and blue circles, respectively. Right, average pallidal and thalamic waveforms—spike 'kernels'—were extracted form the paired recordings and used to construct templates for the spike sorter (see below). (**c**) Detailed methods for template-based spike sorter that detects spike overlaps. The goal of the spike sorter is to create spike overlap 'templates' that simulate spike overlaps occurring in the real data. (1) First, a subset (< 20) of pallidal and thalamic spikes are labeled manually. (2) These spikes are then averaged to create spike 'kernels'. (3–4) A set of templates are constructed as follows: the pallidal and thalamic kernels are summed together with different time lags (e.g. from –1.2 to 1.2 ms in 0.1 ms increments). 7 example templates (3) and a complete set of 26 (4) are shown. (5) An example template (green) is subtracted from each time point of the voltage trace, resulting in a difference vector (6). The difference vector contains discrete minima at the times of template-match (left). The distribution of values for the difference vector yields a bimodal distribution—with the minima corresponding to template-matches (right). The threshold for detection is set by the Fisher discriminant between the two modes of the distribution (dashed blue line). This distribution was computed from the running the example template through 6 seconds of recording data. (7) Template matches are registered as pallidal and thalamic spike times.

Supplementary Fig. 5. Additional examples of simultaneous recordings of pallidal axon terminals and putative post-synaptic thalamic neurons. (**a**) Example of extracellular waveform containing signals from a thalamic neuron (black circles) and a putative presynaptic pallidal axon terminal (red circles). (**b–c**) Instantaneous firing rates of the thalamic neuron (black) and simultaneously recorded pallidal terminal (red) plotted during a bout of adult undirected song (spectrogram shown above, dph 110). (**d**) Expanded view of data from panels b–c, showing the pallidal (red) and thalamic (black) spike trains (top) and the corresponding instantaneous firing rates, which are visibly anti-correlated. (**e**) Raster plot of thalamic spikes (black ticks) aligned to the timing of pallidal spikes (red line) for the data shown in panels b–c. Note that each pallidal spike is followed by a brief period of absolute thalamic spike suppression, and that the duration of this suppression is shorter during singing. (**f–g**) Raster plot, as in e, separated into singing (**f**) and non-singing (**g**) epochs. Data are sorted by the duration of the pallidal interspike interval (ISI), with longer intervals at top. Red line at right shows the time of the next pallidal spike. The plots show 20,000 pallidal ISIs during singing (**f**) and 6,000 ISIs during non-singing (**g**) periods. (**h**) Histograms of thalamic spike probability aligned to the timing of pallidal spikes during singing (blue) and non-singing (black). (**m–p**) Rasters and histograms are plotted (as in panels f–h) for an additional pair recorded in the adult bird (**j**), and four additional pairs recorded in juveniles (**k–p**).

Supplementary Fig. 6. Analysis of paired pallido-thalamic recordings. Spike train cross correlograms (as in Fig. 2f) and IFR cross correlations (as in Fig. 2h) measure

different aspects of the pallidothalamic relationship. (**a**) A pair of hypothetical pallidal and thalamic spike trains, each firing at 100 ± 10 Hz, but with a consistent time-lag of 5 ± 1 ms between the pallidal and thalamic spikes. (**b**) Plot of the spike triggered raster as in Figure 2e. (**c**) As expected, there is a high probability that a thalamic spike will occur around 5ms after the pallidal spike, thus producing a pronounced peak in the spike-train cross-correlation. Note that this peak does not represent a change in thalamic firing rate: This neuron spikes at a constant rate of ~100 Hz (all spike intervals are roughly 10ms). Thus, the peak in this spike-train cross correlation does not represent a firing rate change; rather it emerges because of the precise temporal relationship between the thalamic and pallidal spikes. (**d**) In contrast, the instantaneous firing rate (IFR) illustrates firing rate (inverse of spike intervals) but is insensitive to spike times. In our example spike train, the small fluctuations in firing rate we built into the pallidal and thalamic spike trains were uncorrelated with each other, and this fact is confirmed by the flat IFR cross-correlation. (**e**) Example spike trains that exhibit slow, anticorrelated changes in firing rate (i.e. when the pallidal rate increases, the thalamic rate decreases). (**f**) IFR cross correlation of spike trains shown above, which shows a broad negative peak. In summary, the spike train cross correlation and the IFR cross correlation measure different (and largely orthogonal) properties of the relation between two spike trains.

(**g**) Plot of spike train cross correlation, using the same data as shown in Fig. 2f, but with a larger time bin (bin size = 10ms). Note the clear anticorrelation at zero time. Thus, just as the peak in panel c of the present figure did not signify a rate increase, the peak in the pallido-thalamic cross correlogram in Fig. 2f did not signify a thalamic rate

increase triggered by the pallidal spike, rather there was a net suppression of thalamic activity by pallidal spikes.

Supplementary Fig. 7. Slow rate modulations contribute to the half-width of IFR cross correlations. (**a**) Spike train from a simultaneously recorded pallidal terminal (red) and thalamic neuron (black). Data are from a singing period for the same pallido-thalamic pair in Fig. 2. Note that many pallidal interspike intervals contain thalamic spikes, and that thalamic spikes occur primarily at the end of the pallidal ISI, as shown in Fig. 2d–f. (**b**) The instantaneous firing rates (IFR) of the spike trains in panel a. The IFR at any time is the inverse of interval between the nearest preceding and following spikes (see Methods). Long ISIs (>10 ms) produce long periods of low IFR (blue asterices), resulting in slow modulations in the IFR. (**c**) Autocorrelations of pallidal (red) and thalamic (black) IFRs. The full width at half-maximum (FWHM) of the pallidal and thalamic IFR autocorrelations was 9.2 ms and 9.8 ms, respectively. The widths of the autocorrelations reflect the timescales of the modulations in firing rate. (**d**) The cross-correlation between the pallidal and thalamic IFRs, plotted as in Fig. 2h. Inset, expanded view of the negative peak of the cross correlation. (**e**) The width (FWHM) of the IFR cross correlation plotted against the half-width of the pallidal (red) and thalamic (black) IFR autocorrelation (n = 6 pairs). Note that the width of the IFR cross-correlation is positively correlated with the width of the IFR autocorrelations. This finding explains why pallidal and thalamic IFRs were significantly anti-correlated at positive and negative lags out to ± 100ms. However, this is simply a consequence of the large width (~10 ms) of the DLM and pallidal IFR

autocorrelations. The actual causal influence of pallidal inputs on DLM neurons appears to be extremely brief (milliseconds).

Supplementary Fig. 8. Simulated DLM spiking response to pallidal inputs during singing. (**a**) Syllable onset-aligned rate histogram for 14 pallidal terminals during singing, *red*, and the rate histogram for the predicted thalamic response, *black*, see details on simulation of thalamic response to pallidal inputs below. (**b**) Mean ± s.e.m. of the data plotted in panel a. (**c**) Syllable onset-aligned rate histogram for DLM neurons recorded in subsong birds. (**d–f**) Data are plotted as in panels a–c for syllable offsets.

During singing, the first thalamic spike occurred on average 5.2 ± 0.6 ms after a pallidal spike, and an additional thalamic spike discharged for every 3.9 ± 0.6 ms increase in the duration of the pallidal ISI (data are mean ± s.e.m. for 6 pairs during singing). Based on this relation, we can 'predict' the number of DLM spikes than should occur in any pallidal interspike interval. We used this approach to 'simulate' the DLM spike response to each pallidal spike train recorded in subsong birds (n = 14 pallidal spike trains). We then examined the syllable onset- (and offset-) aligned activity of the simulated DLM spikes. Consistent with the idea that pallidal input strongly suppresses thalamic spiking, in all cases we observed that the pallidal rate increases observed at syllable onsets led to a predicted rate decrease in the thalamic neuron at this time. Similarly, pallidal rate decreases at syllable offsets resulted in predicted thalamic rate increases at this time. In other words, the predicted thalamic firing rate changes were opposite of what was actually observed.

(g–h) The pallidothalamic interaction was different in the period prior syllable onsets and offsets. Of the eight pairs we recorded, two were recorded in subsong-aged birds (<dph 45) that exhibited syllable onset peaks and offset-dips, and one of these pairs was recorded long enough during singing to compare the pallido-thalamic interaction for pre-onset and pre-offset periods. (**g**) Histograms of thalamic spike probability aligned to the timing of pallidal spikes, plotted as in Figure 2f. Latencies computed from data in the 30 ms period preceding syllable onsets (green) were significantly shorter than those computed from the same period preceding offsets (red) ($P < 0.001$, unpaired t-test). (**h**) The number of thalamic spikes that discharge within a pallidal ISI is plotted against the duration of that ISI, plotted as in Figure 2n. Data are from the 30 ms period preceding syllable onsets (green) or offsets (red). Note that the slope of this relation is significantly steeper prior to onsets (0.31 spikes ms^{-1}) than prior to offsets (0.27 spikes ms^{-1}). Data are from the pair plotted in Figure 2.

Supplementary Fig. 9. Stimulation in RA produces short-latency responses in DLM neurons. (**a**) Schematic of the experimental design. (**b**) Reverse microdialysis probes were custom-fabricated to achieve local inactivation of Area X. (**c**) Extracellular spike waveforms from a pallidal terminal recorded in DLM. The recording was maintained during infusion of muscimol (1.5 mg mL^{-1}) into the microdialysis probe in Area X. Numbers at left indicate the number of minutes elapsed since the onset of drug infusion. Note that spiking is abolished within seven minutes after the onset of muscimol infusion. (**d**) Histological verification of placement of the reverse microdialysis probe in Area X (*left*), as well as recording and stimulating electrodes in DLM (*middle*) and RA (*right*),

respectively. (**e**) Four example traces of a DLM neuron response to single-pulse stimulations of RA, rather than the burst stimulations shown in Fig. 5. Note the increase in DLM firing immediately following the RA stimulation. Vertical scale bar: 5 mV; horizontal scale bar: 50 ms. (**f**) Stimulus aligned raster plot of the response shown in e. (**g**) RA-stimulation-aligned rate histogram for the neuron shown in e–f. (**h**) Average peri-stimulus histogram for 9 neurons tested with single-pulse RA stimulation (4 birds, shading indicates ± s.e.m.). Significant responses were observed in 7 of these 9 neurons. (**j–n**) Data are shown as in e–g for experiments where the stimulation electrode was placed outside of RA. (**p**) Average peri-stimulus histogram for 10 neurons tested with single-pulse RA stimulation (3 birds, shading indicates ± s.e.m.). No significant responses were observed.

Supplementary Fig. 10. Distinguishing DLM from DMP in neural recordings. (**a**) DLM was targeted by seeking out the high frequency pallidal terminals as described (see Methods). Voltage traces (2 seconds) from extracellular recordings at 4 sites in DLM are shown. Note the high levels of spontaneous firing. (**b**) Voltage traces from 4 sites recorded in DMP. Note the absence of spontaneous activity. (**c**). MMAN stimulation results in antidromically driven, precisely timed neural activity in DMP (arrows). Each panel is the superimposition of 10 sweeps aligned to MMAN stimulation at the recording sites shown in panel b.

Supplementary Fig. 11. RA axon terminals can be seen spanning DLM and DMP. (**a**) Schematic of experimental design. Cholera toxin β subunit conjugated to Alexa-647

and 555 was injected into MMAN and LMAN, respectively. These injections retrogradely labeled DMP and DLM. Herpes simplex virus (HSV) driving expression of GFP on a CMV promoter was injected into RA, resulting in fluorescently labeled RA axon terminals in the dorsal thalamus. (**b**) To test if the axons that innervate DLM may also innervate DMP, we focused on a region of interest at the boundary of DLM and DMP (light blue square), examples of which are shown in panels d–e and g–h. (**c**) Verification of virus injection into RA and tracer injection into LMAN. CTB-555 anterogradely transported from LMAN, labeling LMAN axon terminals in RA (red). Note the GFP-expressing neurons within RA (green). (**d–e**) Two examples showing RA arborizations in DLM (red neurons) and DMP (blue neurons). In several cases, axons can be seen spanning these two structures. During imaging, the trajectories of individual axons were tracked as they passed from DLM into DMP (distinct axons are labeled with distinct arrowheads). Data are from the left hemisphere of a juvenile bird (dph 44) (**f–h**) Data are shown as in d–e, with examples from the right hemisphere of the same bird.

Supplementary Fig. 12. RA neurons that were not antidromically activated by DLM stimulation exhibited many types of rate modulations relative to song timing. While some RA neurons not antidromically identified as DLM-projecting resembled RA_{DLM} neurons, exhibiting rate increases and decreases prior to syllable onsets and offsets, respectively (n = 22), many exhibited firing rate modulations never observed in RA_{DLM} neurons. Shown in this figure are two examples of RA neurons recorded during subsong that exhibited such patterns of activity: rate peaks that occurred immediately prior to syllable offsets (n = 22), or immediately following syllable onsets (n = 12). (**a**)

Extracellular voltage trace and the instantaneous firing rate of an isolated RA neuron recorded during subsong (spectrogram shown above, dph 49). (**b**) Expanded view from the period marked by a gray bar in panel a, showing neuronal activity that increases prior to syllable offsets. (**c**) Syllable offset aligned rate histogram for the neuron in shown in panel a (top) and for 22 RA neurons that similarly exhibited peaks of neuronal activity prior to syllable offsets (bottom, shading indicates ± s.e.m.). (**d**) Extracellular voltage trace and the instantaneous firing rate of an RA neuron recorded during subsong (dph 47). (**e**) Expanded view from the period marked by a gray bar in panel d, showing activation of this RA neuron after syllable onsets. (**f**) Syllable onset-aligned rate histogram for the neuron shown in panel d (top) and for 12 RA neurons that similarly exhibited increases in neuronal activity following syllable onsets.

REFERENCES

1. Goldberg, J.H., Adler, A., Bergman, H. & Fee, M.S. Singing-related neural activity distinguishes two putative pallidal cell types in the songbird basal ganglia: comparison to the primate internal and external pallidal segments. *J Neurosci* **30**, 7088-7098 (2010).
2. Olveczky, B.P., Andalman, A.S. & Fee, M.S. Vocal experimentation in the juvenile songbird requires a basal ganglia circuit. *PLoS Biol* **3**, e153 (2005).

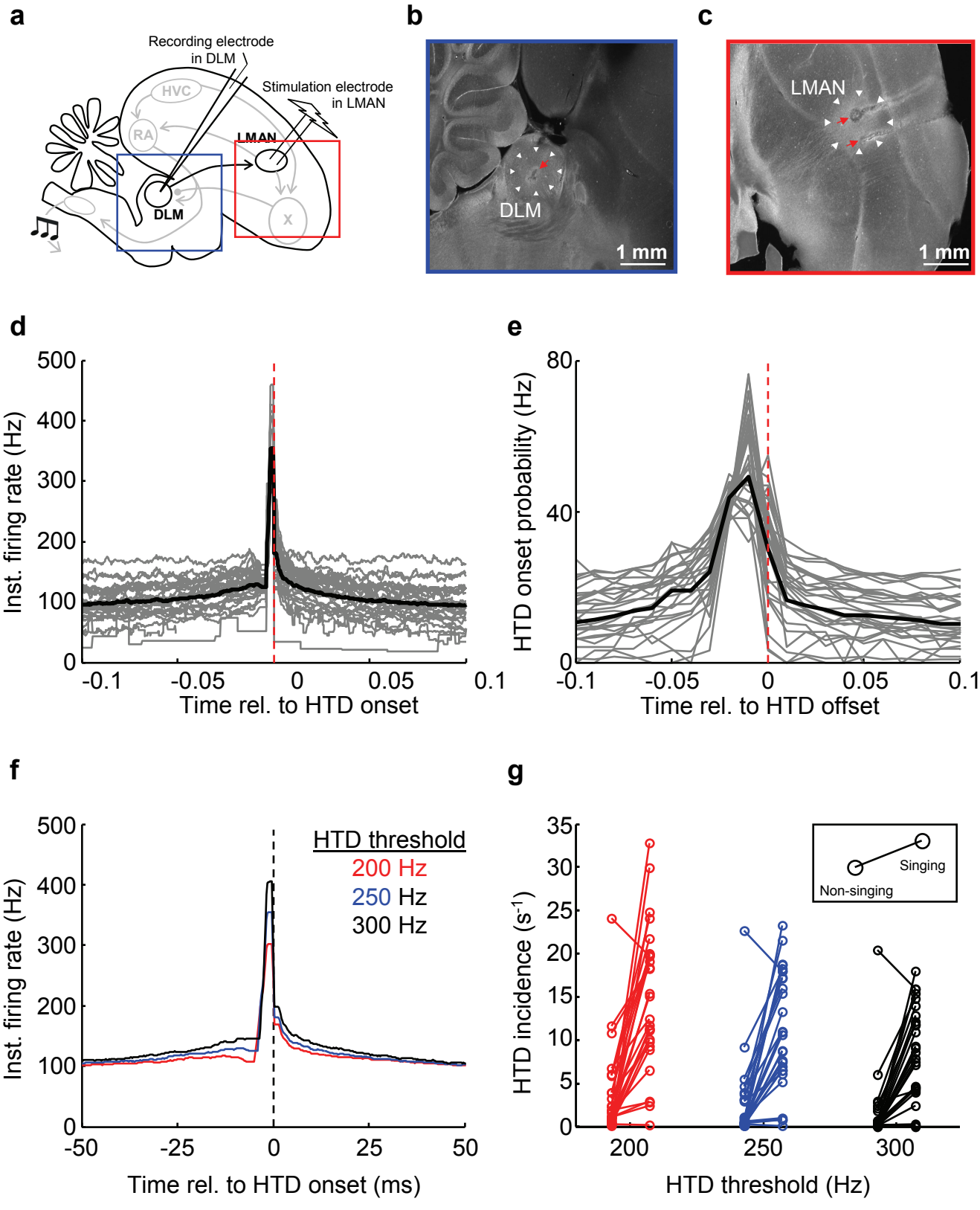

Supplementary Fig. 1

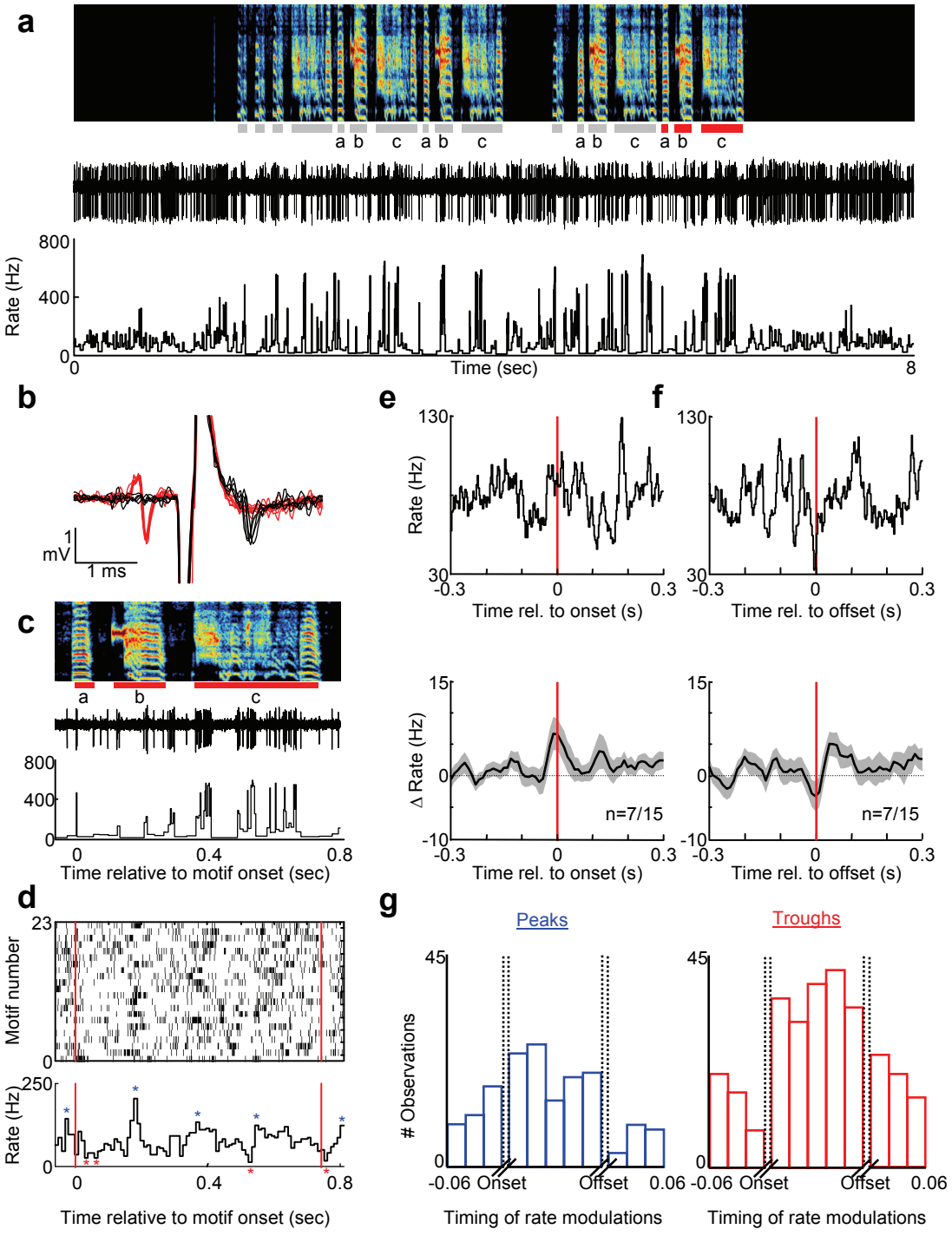

Supplementary Fig. 2

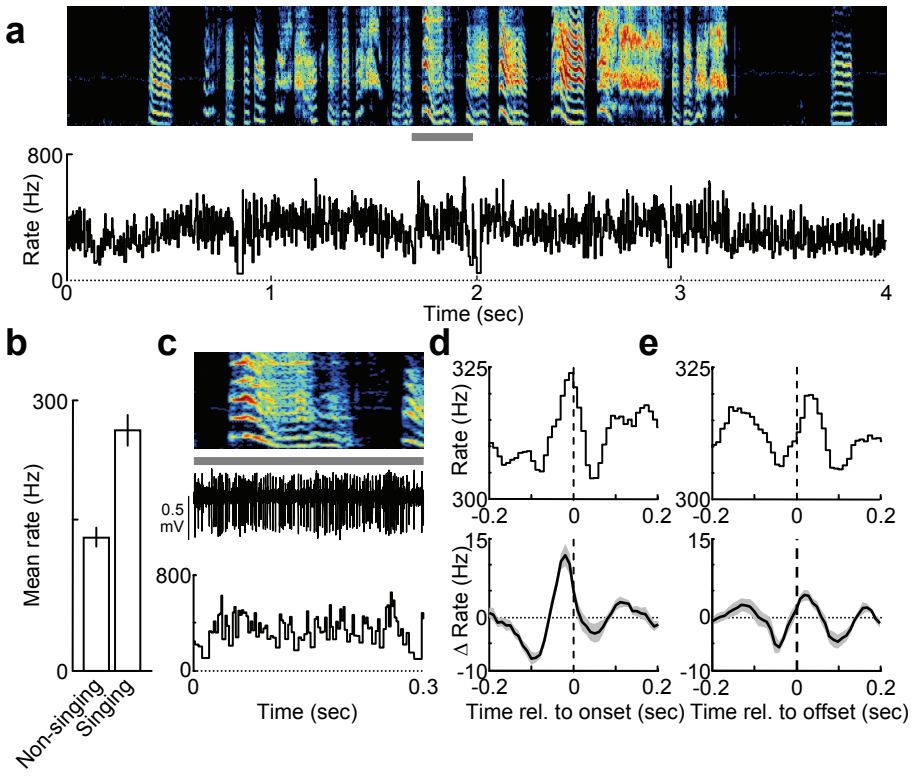

Supplementary Fig. 3

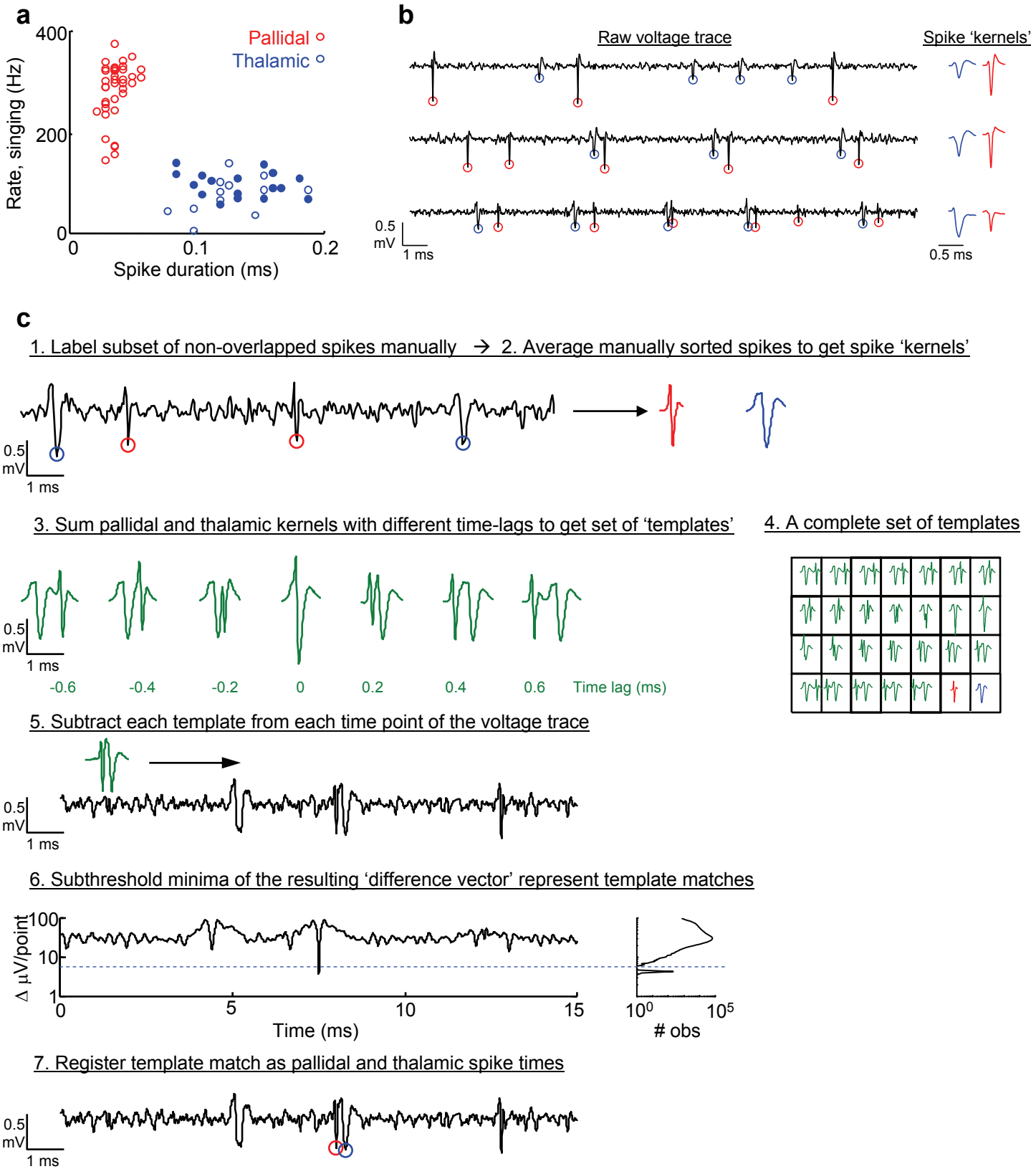

Supplementary Fig. 4

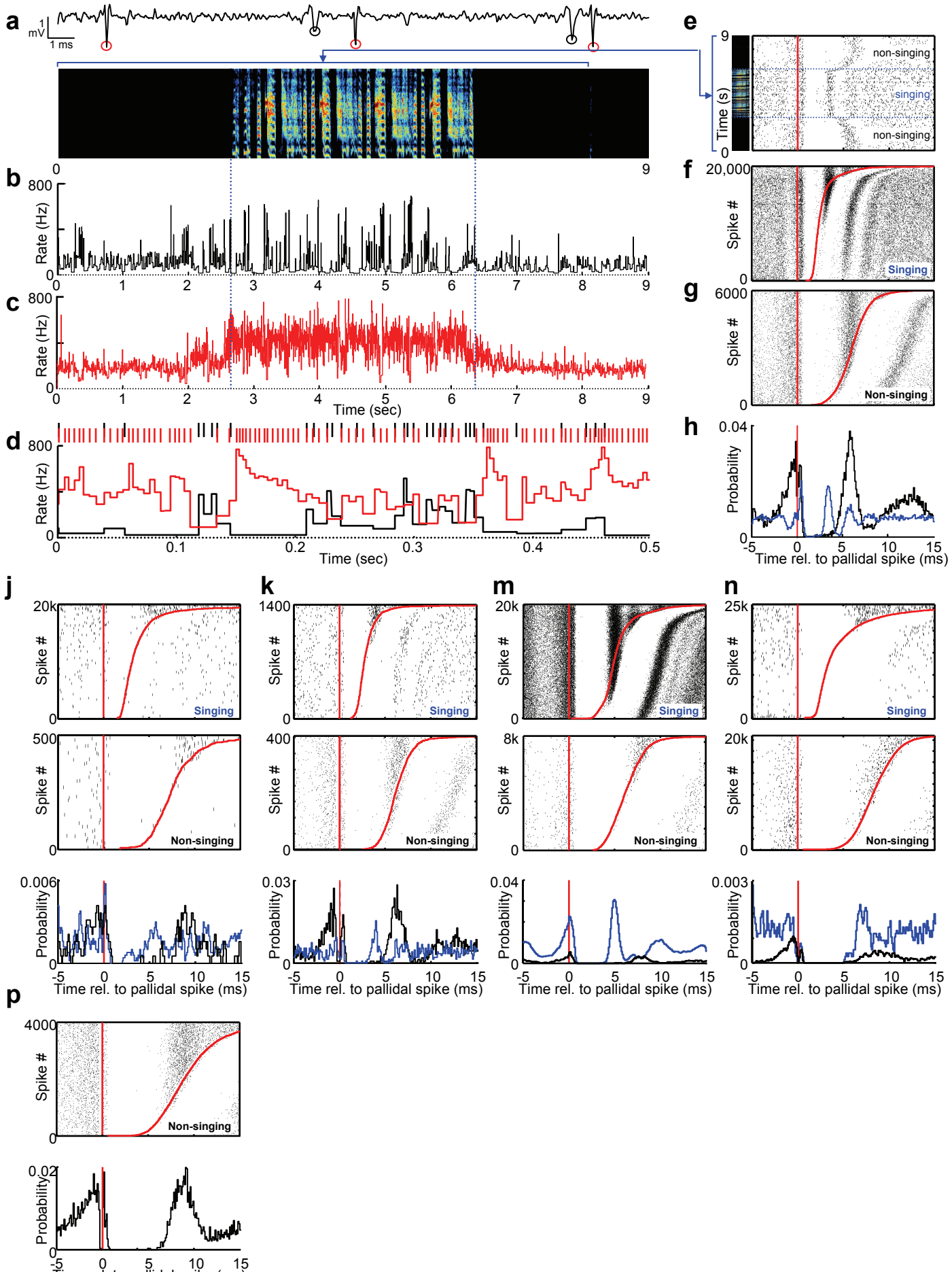

Supplementary Fig. 5

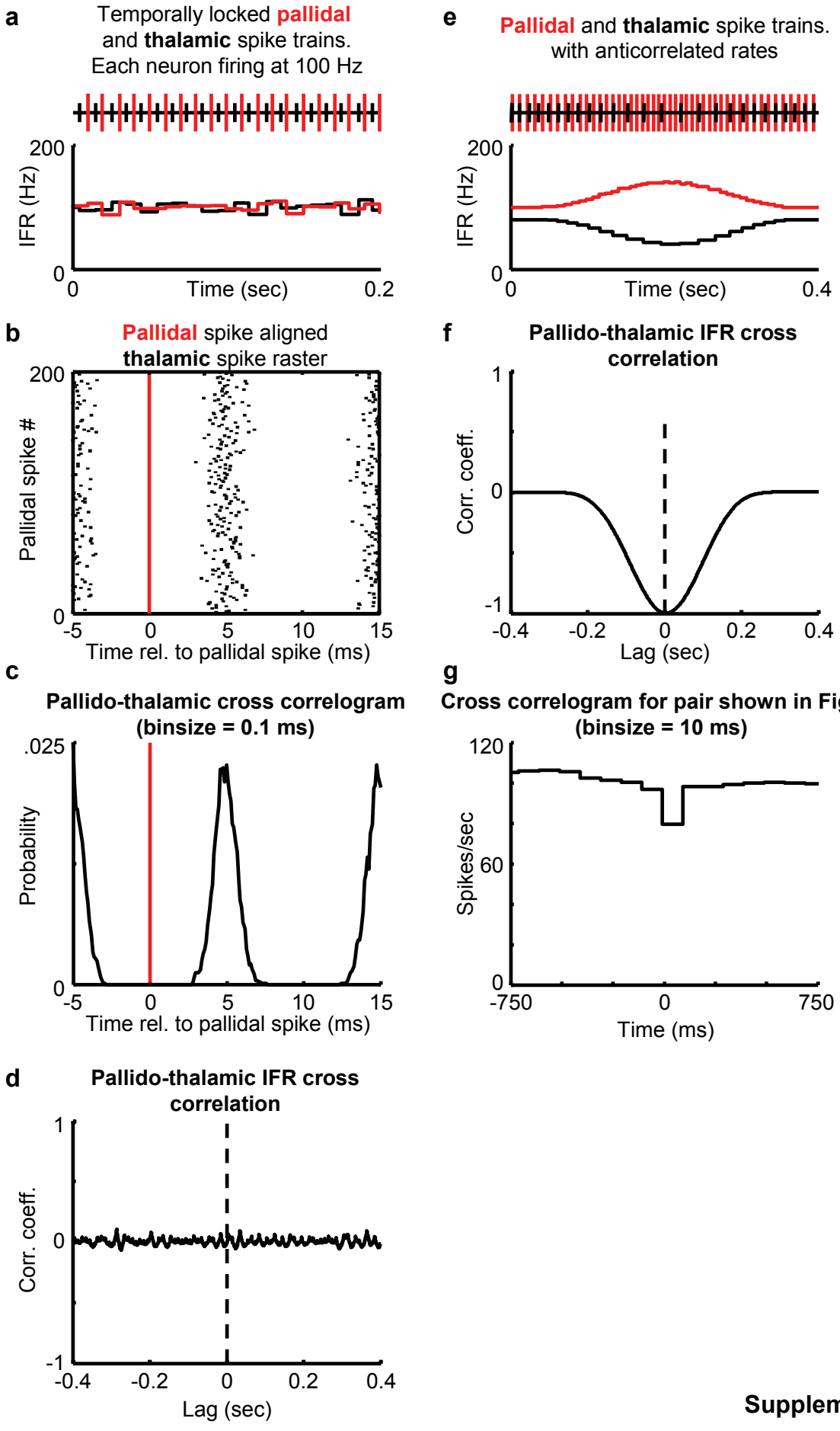

Supplementary Fig. 6

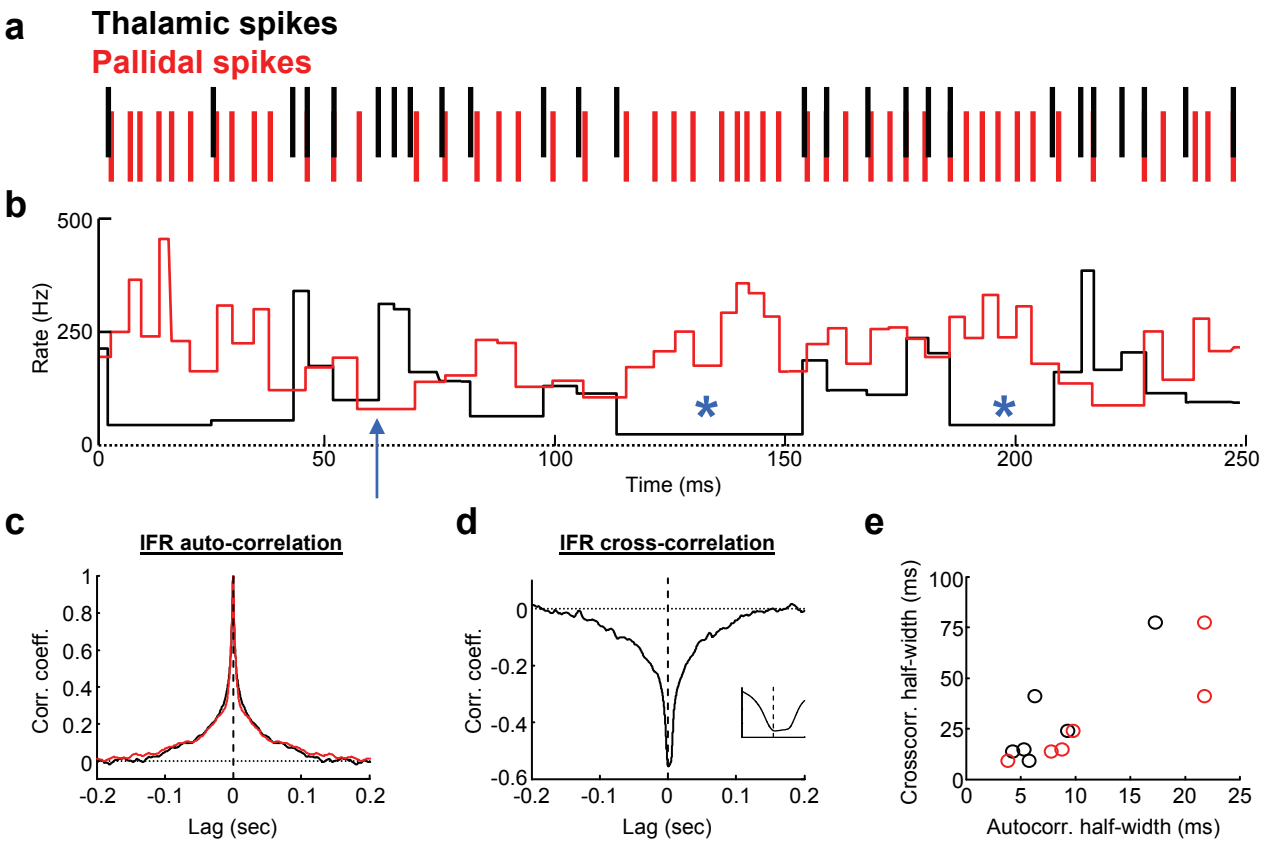

Supplementary Fig. 7

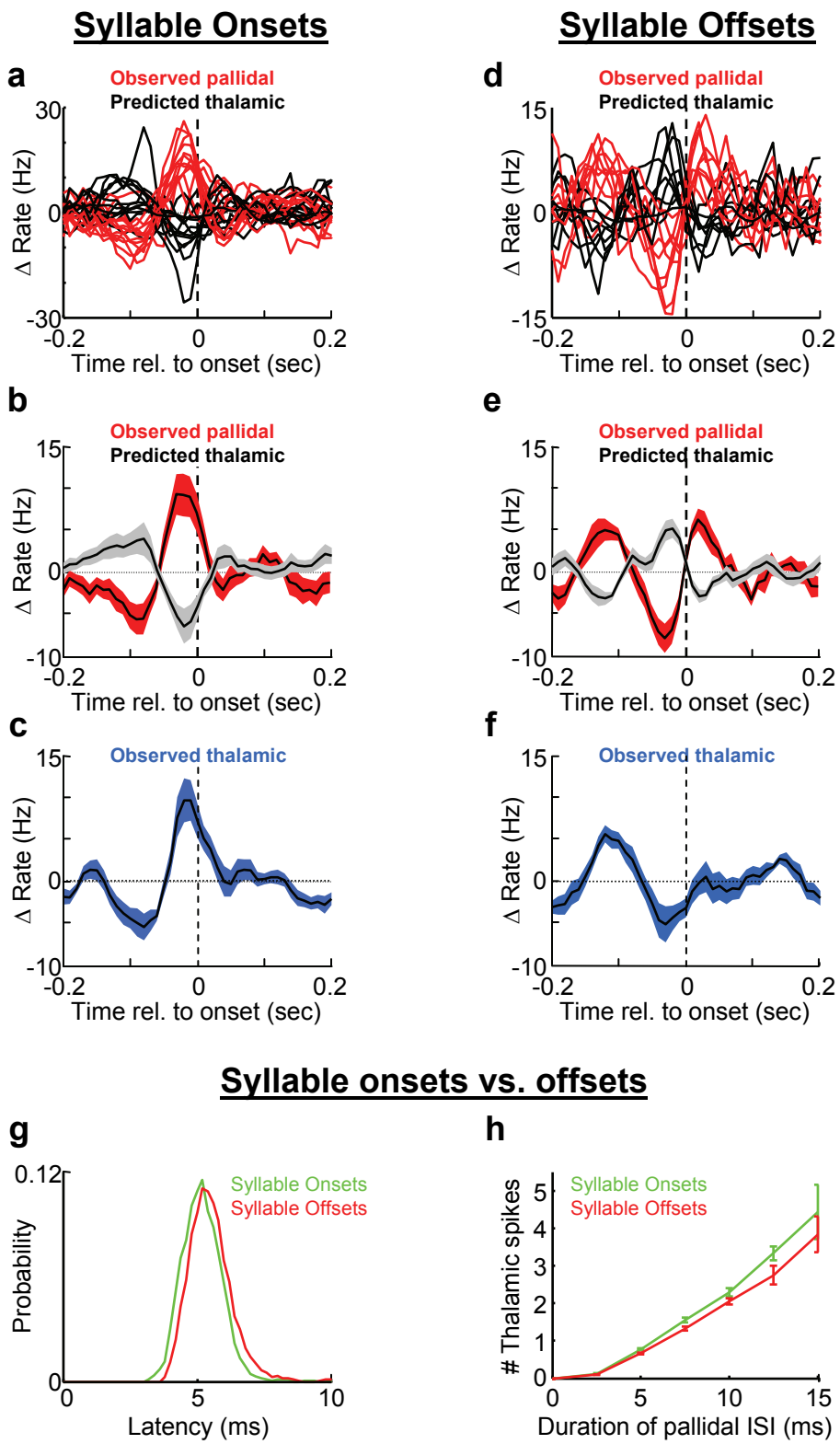

Supplementary Fig. 8

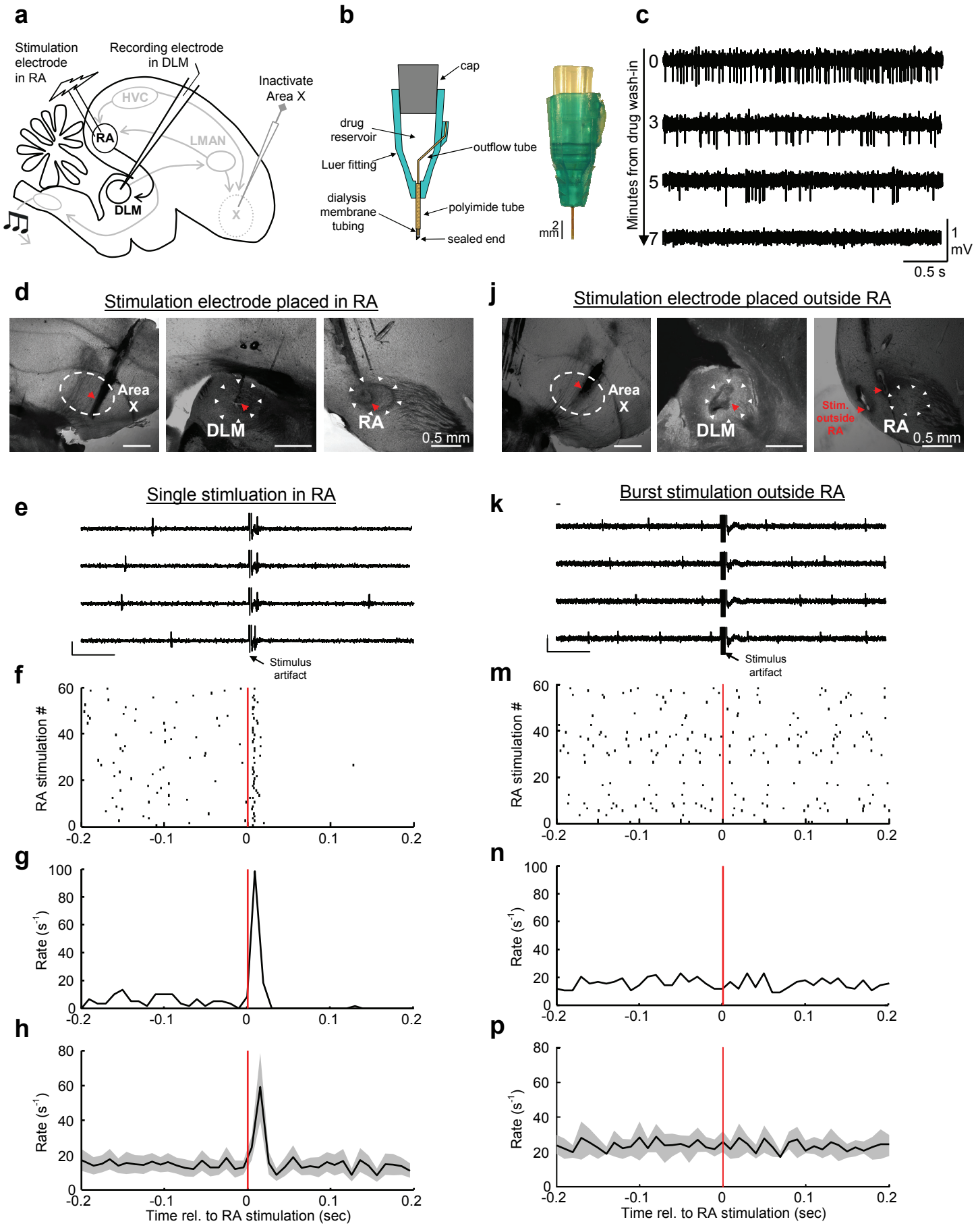

Supplementary Fig. 9

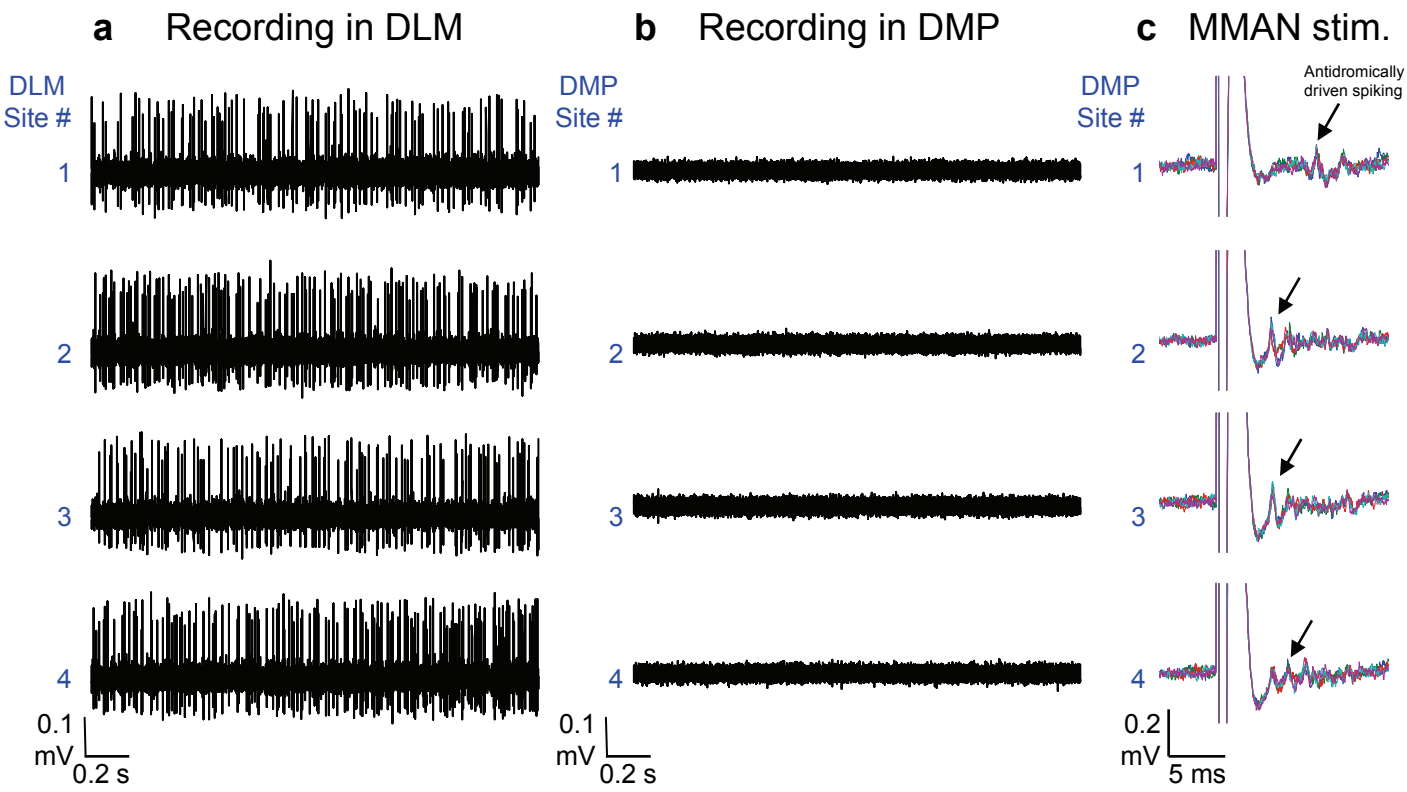

Supplementary Fig. 10

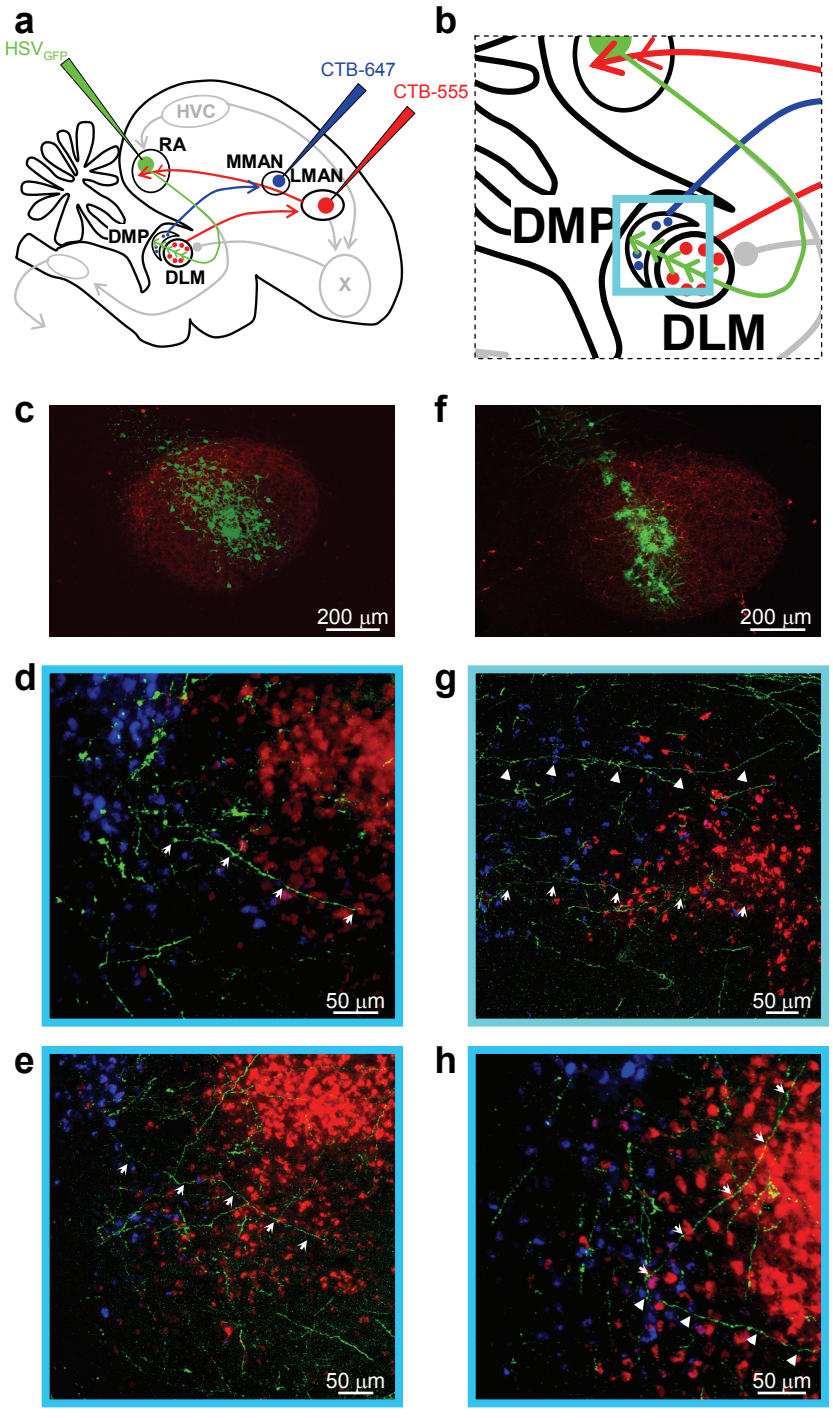

Supplementary Fig. 11

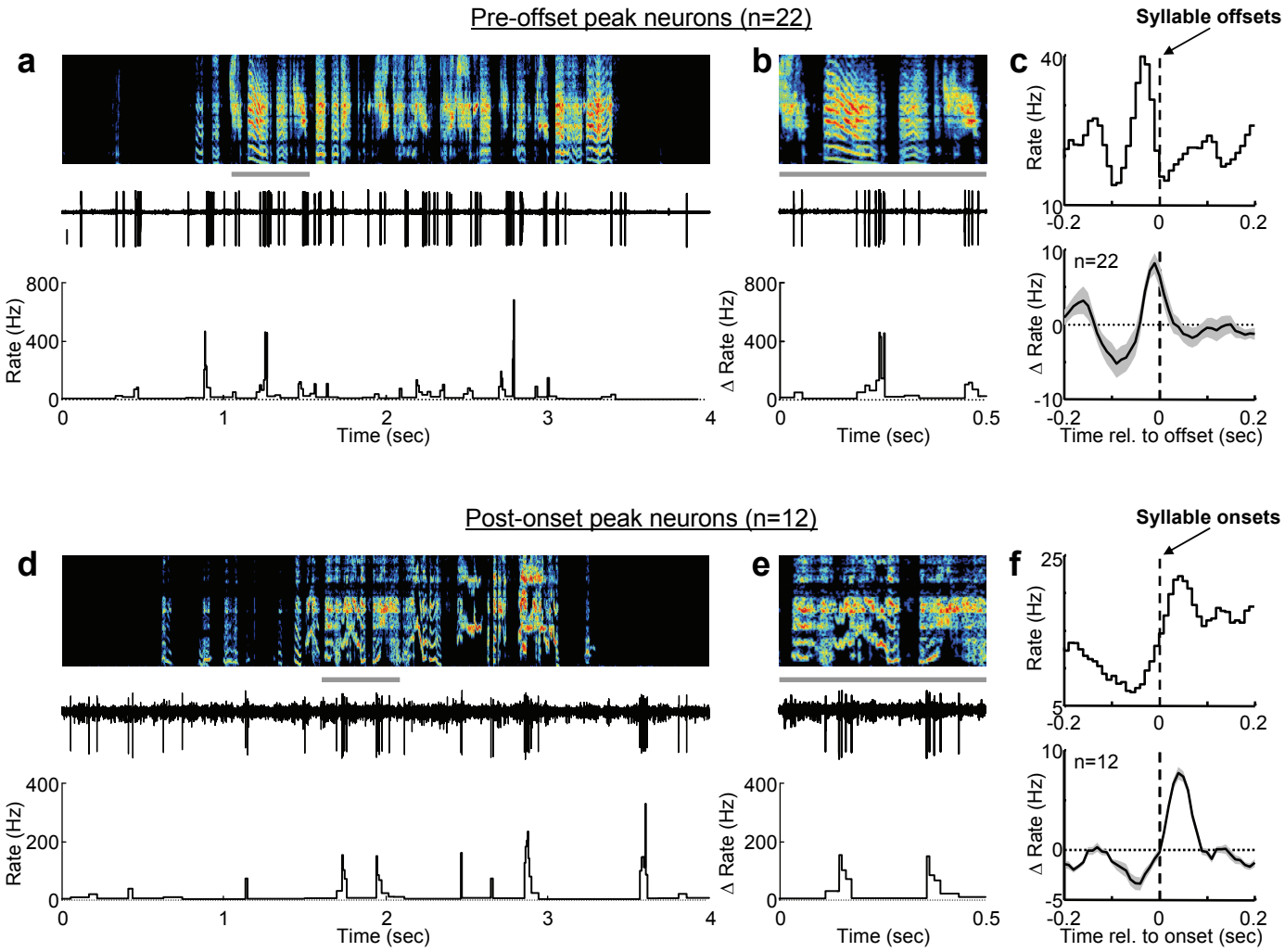

Supplementary Fig. 12